June 2020 Journal of Soils and Sediments
DOI: 10.1007/s11368-020-02691-3

Analysis of deep-ocean sediments from the TAG hydrothermal field (MAR, 26°N): Application of short-wave infrared (SWIR) reflectance spectra for offshore geochemical exploration

Jelena Milinovic[1] · Fernando J.A.S. Barriga[2] · Bramley J. Murton[3]

[1]REQUIMTE/FCT-NOVA, Faculty of Sciences and Technology, Nova University of Lisbon, Lisbon, Portugal.
[2]Institute Dom Luiz, Faculty of Sciences, University of Lisbon, Campo Grande, Lisbon, Portugal.
[3]National Oceanography Centre, European Way, Southampton, England.
(Corresponding author: j.milinovic@fct.unl.pt)

Abstract

Purpose The cost-efficient methods of analysis, such as rapid short-wave infrared (SWIR) spectral analysis have been applied for the efficient exploration of critical raw materials (CRM), including mineral components and rare earth elements (REE) from the deep-ocean sediments.

Methods Gravity cored sediment samples were collected during an oceanographic mission to the Trans-Atlantic Geotraverse (TAG) hydrothermal field of the Mid-Atlantic Ridge (MAR, 26°N). SWIR reflectance spectra (dependent variable) of samples were mathematically tested against referent geochemical data (independent variable), obtained by conventional analysis (ICP/OES, ICP/MS), after applied full cross-validation multivariate partial least square regression (CVPLSR). Value of parameter - residual predictive deviation (RPD) was used for evaluation of CVPLSR modeling: RPD > 2.5 (satisfactory calibration model for the screening purposes), and RPD > 5.0 (model adequate for the quality control of the studied elements).

Results The CVPLSR modeling provided significant results for the determination of several mineral components: major elements (Fe, and Si) had the values of RPD equal to 3.65 and 2.84, respectively indicated a viable potential for their routine analysis, whereas RPD for Ca was equal to 5.51, thus assured its quality control by SWIR analysis, in sediment samples of studied location. Among the REE, Ce (RPD = 2.55) and Er (RPD = 2.59) yielded the most satisfactory results.

Conclusions The findings highlight the benefit of rapidly obtained empirical SWIR-reflectance data, which can be used for near-real-time exploration of geochemical deposits hosted in deep-ocean sediments.

Keywords TAG hydrothermal field · Deep-ocean sediments · Rare earth elements (REE) geochemistry · Short-wave infrared (SWIR) spectra · Cross-validation partial least square regression (CVPLSR) · Residual predictive deviation (RPD)

1 Introduction

Current technological demands are rapidly increasing the global needs for critical raw materials (CRM), including mineral components and rare earth elements (REE), that are generally in short supply, particularly in Europe (Coulomb et al. 2015; Blengini et al. 2017). According to the most recent data of the European Commission (EC), in 2017 the CRM including both light (La-Sm), and heavy rare earth elements (Eu-Lu) together with Y, were listed with a maximum supply risk (EC 2017). The parameter 'substitution index' defined in the EC report as a measure of difficulty in substituting the material, was scored (for both economic importance and supply risk) with the highest values (0.9 - 1.0) for all REE. At the same time, China as a monopoly producer of the REE is the major consumer of these materials resulting in a danger to the secure supply to the European industry. This fact together with the critical role of rare earths application in the industry, technology, and medicine, created an urgent need for rapid exploration of natural resources of the REE (Emsbo et al. 2015; Giese 2018).

A significant contribution to future raw material supply could be deep-ocean mineral deposits, including seafloor massive sulfide (SMS) deposits (Barriga 2017; Lusty and Murton 2018). Hydrothermally active mineral deposits, located in the Trans-Atlantic Geotraverse (TAG) area, occur a few kilometers from the current spreading axis of the Mid-Atlantic Ridge (MAR) at 26°N (Lusty and Murton 2018; Murton et al. 2019). Current hydrothermal activity in this area is characterized by the discharge of high-temperature fluids, the deposition of polymetallic sulfide, and the presence of unusual vent-related biota (Rona et al. 1986; Campbell et al. 1988; German et al. 1993; Lusty and Murton 2018). The neutrally buoyant plume overlying the TAG hydrothermal field is characterized by abundant fine-grained Fe-oxyhydroxide particles

enriched in Cd, Cu, Ni, Pb, and Zn, which are efficient REE scavengers (Thompson et al. 1985; German et al. 1990). Elsewhere, the TAG hydrothermal field hosts many extinct SMS deposits. These are several thousands of years old and no longer discharge hydrothermal fluids but may host microbial vent fauna (Van Dover 2019). They are covered by sediments that include metalliferous and carbonate and have aprons of mass wasted material around them.

Sediments, derived from deep-ocean mineral deposits, can serve as vectors to mineralization by their rapid analysis. One approach being considered is the development of new and alternative mineral deposits, such as inactive SMS, requiring innovative exploration techniques. As a potential solution, portable infrared mineral analyzers (PIMA) can be used as a method of choice for the rapid, cost-efficient short-wave infrared analysis (SWIR) of mineral components and REE-bearing minerals in numerous land-based environmental samples, as well as deep-ocean sediments. A small amount of sediment sample material enables fast acquisition of SWIR-spectra, which describes the patterns of reflected electromagnetic radiation in the wavelength range of 1300 - 2500 nm (Clark et al. 1990; Horsfall 1999). The SWIR-spectra is sensitive to stretching and bonding vibrations characteristic of several molecule/functional groups in mineral crystal lattices, such as: -OH and H_2O (1350-1550 nm), -OH (1750-1850 nm), H_2O (1900-2000 nm), Al-OH (2150-2250 nm), Fe-OH (2250-2300 nm), Mg-OH and/or carbonates (CO_3^{2-}) (2300-2350 nm) (Horsfall 1999). These groups are common components of many hydrothermal mineral species such as kaolinite, illite, smectite groups, as well as many carbonates.

REE also absorb in the short-wave infrared region, typically with sharp and narrow absorption features that are mainly attributed diagnostically to the presence of individual elements arranged in the crystal lattice of minerals (Horsfall 1999). However, a notable lack in knowledge exists in the field of reflectance spectroscopy of REE mineralogy. The recent results showed that some REE-bearing minerals can be identified by reflectance spectroscopy in a short-wave infrared region which depends primarily on the concentration of the lanthanide ion (Turner et al. 2014; Turner et al. 2016; Lorenz et al. 2019). Consequently, diagnostic features related to REE-vibrational bands are quite difficult to register, because in the SWIR-region more abundant mineral-components (for ex., Al-OH, Fe-OH, Mg-OH, CO_3^{2-}) absorb as well, as previously explained.

Although PIMA is unable to distinguish particular mineral components in mixtures, which depends on the content of each mineral, the degree of crystallinity, and the strength of the specific mineral-element and/or -group absorption feature (Sun et al. 2001; van Ruitenbeek et al. 2012), in this work we report the use of PIMA to acquire SWIR-data for rapid analysis of mineral components, in gravity cored sediment samples surrounding inactive SMS deposits. In this contribution, the objective was to provide a better understanding of seafloor major- and REE- mineral components in deep-ocean sediments by comparing the spectra with the independently acquired data (concentration of elements), and by combining it with meaningful relationships between geochemical variables. It should be emphasized that these data are scarce in the literature and do not provide a good basis of comparison.

The aim of our research is the prediction of geochemical variables from rapid, exploration-oriented, integrated SWIR-spectral data of deep-sea sediments surrounding inactive SMS deposits with full cross-validation partial least square regression (CVPLSR) for modeling. Established models, based on mathematical relationships between reflectance spectra and geochemical data, can be used as a pattern for the future rapid exploration of geochemical resources based on offshore SWIR-reflectance analysis.

2 Materials and methods

2.1 TAG-sediment samples

Sixty-five sediment samples, collected from 13 gravity cores recovered from between 3407 m and 3654 m in the TAG hydrothermal field (26°N, Mid-Atlantic Ridge), were selected for this study (Fig. 1). Most of the cores in the vicinity of the hydrothermal mounds are iron-rich and hence show evidence of hydrothermal influences. These are from: Shimmering mound (GC: 626, 681, 682); proximal to Southern mound (GC-702, 100 m SW and SE of the inactive Shinkai and Double mound, respectively and GC: 627, 644, 703), near MIR zone (GC: 649, 692) and 800 m to the NW of the high-temperature active TAG mound (GC-693), whereas three cores exhibited highly-carbonate contents (GC: 615, 1200 m SE of the MIR zone and GC: 616, 617, proximal to Rona mound) (Fig. 1).

All sediments were collected by gravity core (GC) during the six-week oceanographic mission ('M127') in May-June, 2016 on the research vessel, 'Meteor' (Petersen 2016; Petersen et al. 2017; Milinovic et al. 2020). Briefly, upon recovery, gravity cored sediments were cut into 1-m long sections, and the ends were sealed with caps. The core sections were split longitudinally using a hand-held, power disc-saw, split with a wire cutter in two halves and photographed. A portion of sediment was sampled from the center of the

working half, using open syringes as pistons, and stored in sealed polypropylene sleeves, previously flushed with N_2 to prevent sulfide oxidation (Petersen 2017).

For infrared analysis, subsamples were dried and ground onshore. Sample drying is time-consuming step, since the temperature should not exceed 40 ºC, to prevent destruction of the clay mineral structure and hence preclude a bias in the SWIR analysis. On average, about 5 hours were enough for drying the samples until constant mass. Samples were ground in an agate mortar and pestle, without any further pre-treatment step. The grinding step was accelerated by using ethanol (a few drops) until no asperity was felt.

Several of the cores showed evidence of hydrothermal influence and alteration products and representative samples were selected for this study, as an example, more than 30 samples were selected from core GC-627, proximal to Southern mound (Fig. 1).

2.2 Geochemical analysis of TAG-samples by peroxide fusion - ICP/OES and ICP/MS

TAG-sediment samples were analyzed for total major and minor elements (Al, Ca, Cu, Fe, K, Mg, Mn, Pb, S, Si, and Zn) and REE (Ce, Dy, Er, Eu, Gd, La, Nd, Pr, Sm, Y, and Yb) in ISO 17025 accredited Activation Laboratories Ltd. (Actlabs, Canada) (Actlabs 2019). The total digestion of samples was performed by sodium peroxide fusion method, which was suitable for this purpose because the analysis of Na was not required. Each sample was oxidized with sodium peroxide at 650 °C in zirconia crucibles, and the resulting fusion cake was dissolved in aqueous nitric acid and then diluted to provide concentrations appropriate for quantification by inductively coupled plasma spectrometry optical emission spectrometry (ICP/OES) or by inductively coupled plasma mass spectrometry (ICP/MS), using the instrument Varian 735ES ICP and Perkin Elmer Sciex Elan 9000 ICP/MS, respectively.

ICP/OES and ICP/MS were applied depending on the limit of detection (LOD) for each element analyzed. Namely, detection limits of Al, Ca, Mg, S, and Si were 0.01%, whereas, for Fe, and K, they were 0.05% and 0.1%, respectively (referred to weight percentage, wt.%). For most of REE (Er, Eu, Gd, Pr, Sm, Y, and Yb) the LOD was 0.1 ppm, whereas for Dy it was 0.3 ppm and for La and Nd 0.4 ppm. LOD of 0.8 ppm was obtained for Pb and Ce. In the case of Cu, Mn, and Zn, higher values of detection limits were registered, i.e., 2 ppm, 3 ppm, and 30 ppm, respectively. Hence, Al, Ca, Fe, K, Mg, S, and Si were analyzed by ICP/OES, and in the case when their concentration was higher than 10,000 ppm, Cu and Mn were also analyzed by the same technique. The rest of the elements were analyzed by ICP/MS. To assure quality control of ICP analysis, at least ten certified reference materials were used for each required analyte. Thus, CRMs -OREAS (spec.: 131a, 101a, 98, 13b, 922, 621) were used for quality control of the analysis of all elements, whereas -GBW (spec. 07239) was used for the analysis of Mn, Pb, Zn, La, Nd, Pr, and Y; -MP (spec. 1b) for the analysis of: Ca, Cu, Fe, Mg, Pb, S, Si, and Zn; and -GXR (spec.: -1, -4, -6) for the analysis of: Ca, Fe, K, Mg, and S.

2.3 Short-wave infrared analysis of TAG-samples

The field portable spectrometer (Integrated Spectronics PIMA-II Instrument, Baulkham Hills, Australia) was used for the reflectance analysis of dried sediment samples in the short-wave infrared (SWIR) region, from 1300 to 2500 nm, with a spectral resolution of 7 nm and a sampling interval of 2 nm, yielding 601 data channels.

The infrared radiation illuminates the dried sample, placed in a glass Petri dish centered over the instrument's viewing port and covered by a dark box in order to eliminate potential interference from external light. Radiation that is not adsorbed by the sample is reflected back to the instrument where a monochromator splits the IR-light into a spectrum. The total measurement time was about 40 seconds and the measuring was performed by two consecutive scans: the first one measured the intensity of radiation reflected from the mineral sample placed in Petri dish, whereas the second scan was performed on the gold reference measures. Thus the PIMA completed scan and displayed the resulting spectrum of the sample. Dark samples have a low reflectance, resulting in poor spectra with high background. Hence, for analysis of dark samples, integration time was set at maximum level, i.e., increased by a factor of 32, to improve the signal to noise ratio. In this case, the measurement time for obtaining a full spectrum was about 2 min.

Short-wave infrared spectra were obtained and stored in the software Pimaview 3.1 Integrated Spectronics (1999), as fos.files and then, they were analyzed by PIMA 'Identify' software, developed 'in-house', for spectral pre-treatment and processing (Carvalho and Barriga 2000). Normalization of spectra was performed by scaling to 100%. The collected spectra were pre-treated by smoothing operation by a Savitsky-Golay technique (with minimum of 5 points). A spectral background was removed from each of the smoothed spectra to derive so-called hull-quotient spectra. The hull-quotient was applied to visualize the small absorption features. As an example, original, raw and hull-quotient subtracted spectra of sample GC-627/B-175, were shown in Fig. 2. It can be seen, that original, untreated reflectance spectrum showed

very low intensity of typical features and, hence, the recognition of characteristic groups can be difficult. After background removal and normalising spectra to 100% of the maximum reflectance value, hull-quotient spectrum is derived, with better defined bands, i.e., sharper and more intense, and therefore their identification became more reliable. Deep diagnostic absorption features of water absorbed on the sample, or as the part of lattice, at 1435, 1910, and 2295 nm became more intense and sharper in hull-quotient spectra. The mean hull-quotient spectrum of three measurements for each sample was used for further processing and mathematical modeling.

2.4 Statistical analysis: Application of full cross-validation partial least square regression

An unsupervised qualitative method of principal component analysis (PCA) using the Unscrambler™ software (v. 10.4, Camo, Norway), was performed on collected data expressing geochemical components (independent variables), for the classification of sediment samples (grouping variable), according to their localization in the TAG area. The purpose of this statistical method was to check the distribution of variables and to correlate them from the score and loading plots. The score plots, shown later, indicate how the samples were plotted along each model component (PC) and how they can be used to cluster similar sample patterns. The loading plots show that the variables are concentrated into several PCs. By understanding the loadings it can be understood how each variable contributes to the prediction model, thus giving better interpretation of the variables relationship in the model.

The SWIR-reflectance spectra were exported to Unscrambler™, to perform multivariate regression analysis. The full cross-validation partial least square regression (CVPLSR) was applied to data using the nonlinear iterative partial least squares (NIPALS) algorithm, with applied Hotelling's T^2 outlier estimation ($P < 0.05$). Since the available dataset was relatively small ($n = 65$), in model input the maximum number of components used was 7, thus assuring more reliable CVPLSR-model. The statistical parameters used to explain the fitness of the quantitative multivariate model were: latent variable (LV), the coefficient of determination (R^2) and root mean square errors for calibration (RMSEC) and cross-validation (RMSECV) data sets. The values of RMSEC and RMSECV are in the same units as the response variables expressed for each element in % (referred to wt.%) or in ppm (Table 1). To describe goodness of the model, the residual predictive deviation (RPD) was used, as an indicator of the quality of the calibration model (Williams and Sobering 1993). RPD corresponds to the ratio between standard deviation (SD) of results obtained by conventional method, ICP/OES and ICP/MS (independent variable) and the corrected standard error of the prediction of the calibration and cross-validation (SEC and SECV, respectively). The value of RPD higher than 2.5 designate satisfactory calibration model for the screening purposes, whereas those higher than 5.0 describe a model adequate for the quality control of component in the studied samples.

3. Results and discussion

3.1 Geochemistry of TAG-sediment samples

Mineral component concentrations measured in the sediments are listed in Table 1. The concentrations of Al and Mg were in ranges of 0.01% - 4.5%, and 0.1% - 2.5%, respectively. Their highest contents were found in samples originated near Shimmering mound (GC: 681, 682) and MIR zone (GC-649). In recent XRD-study, the authors identified Ca (calcite) and Si (quartz) as major mineral components in most of the hydrothermal samples near Shimmering mound (GC: 681, 682), Rona mound (GC: 616, 617) and MIR zone (GC: 615, 649) (Milinovic et al. 2020). K was found in similar average content like Mg, equal to 0.6%, and the corresponding K- and Mg- clay minerals such as illite, and montmorillonite, have been identified in low abundance in highly-carbonated sediment samples proximal to Southern mound (GC-627/B-184), MIR zone (GC-649/B-45) and Shimmering mound (GC: 681/A-250, 682/C-10, 682/C-78) (Milinovic et al. 2020.

Similar to Fe (minerals: goethite, hematite and pyrite), which was found at maximum level of 30% in vicinity of Southern and Shimmering mound, Cu (chalcopyrite) was also detected in higher concentration levels (> 10,000 ppm) in Southern (GC: 627, 702) and Shimmering mound (GC: 681, 682). In the cored samples near the hydrothermal influence (Shimmering mound and TAG active mound), another Cu-sulfide mineral, covellite was detected (Milinovic et al. 2020). Relatively rare Cu-bearing mineral, paratacamite [$(Cu,Zn)_2(OH)_3Cl$] was identified in samples near Shinkai mound (Milinovic et al. 2020).

Lower concentration of Mn was found in cored sediment samples (at depths below seafloor > 210 cm) proximal to Southern mound, ranging from 40 to 450 ppm. In majority of the other samples, concentration of Mn was high (> 1,000 ppm), and in the samples cored near Shimmering mound (GC: -626: A/75, A-95, CC), very high amounts of Mn were detected (> 10,000 ppm) which can be associated with ferromanganese (Fe-Mn) concretions at the MAR, predominantly composed of Mn-oxides, i.e., minerals: todorokite and

birnessite, and a variety of non-crystalline Fe oxyhydroxide (German et al. 1993; Hein et al. 2013; Lusty and Murton 2018; Milinovic et al. 2020). The presence of the Mn-oxide mineral birnessite was also confirmed in samples GC-682: A-185 and A-209, proximal to Shimmering mound (Fig. 1). Sedimentary Mn-enrichment is attributed to transport of Mn-oxide *via* slumping processes (Mills et al. 1993). In pelagic (REE-rich) sediments, Mn-oxides (e.g., todorokite) are mainly presented in the form of micronodules (Elderfield et al. 1981).

The range of concentrations of the REE in the selected samples is presented in Table 1. In comparison to major and minor elements, the content of REE was several (up to 4) order lower. As the most abundant of the naturally occurring REE, cerium (Ce) (crystal abundance of 60 ppm) (Christie et al. 1998), was found in the highest concentrations in selected TAG-samples. Namely, the highest concentrations detected for Ce, were up to 35 ppm in samples proximal to MIR zone, and up to 28 ppm and 31 ppm in Shimmering and Rona mounds, respectively. In samples near Shimmering mound, the abundance of yttrium (Y) was also relatively high, i.e., with its maximum level of 26 ppm, whereas in Rona mound and Mir zone it was 24 ppm. Lanthanum (La) and neodymium (Nd) were the most abundant in samples from Shimmering mound (GC: 681, 682), Rona mound (GC: 616, 617) and MIR zone (GC: 615, 649), where their concentrations did not vary a lot.

On the other hand, in the samples near Southern mound, i.e., GC-627 and GC-644, the variation of both, La and Nd concentration was significant, more precisely in intervals: 0.4 - 19 ppm, 0.4 - 7 ppm and 0.9 - 19 ppm, 0.4 - 7.3 ppm, respectively. The lowest concentrations of both light rare earth elements were detected in the bottom samples of the cores proximal to Southern mound (GC: 627/A-284 and 644/A-225).

For the rest of the REE, the maximum concentrations were less than 7 ppm. Namely, the highest concentration of 6.7 ppm was found for gadolinium (Gd), 4.8 ppm for both dysprosium (Dy) and praseodymium (Pr), and 4.3 ppm for samarium (Sm) (Table 1). Eu was detected in the average concentration of 1 ppm, whereas the lowest abundance was detected for ytterbium (Yb), in a concentration interval of 0.1 - 2.2 ppm, with an average of 0.9 ppm. (Only the concentration levels of the mineral components and REE that gave a good statistics for the studied CVPLSR-model are presented in Table 1).

3.2 Short-wave infrared reflectance spectral data of TAG-sediment samples

SWIR-analysis shows that most of the samples are characterized by two features: at 1440 and 1940 nm of wavelengths. The 1440 nm peak is associated with hydroxyl (-OH) group bonds in water molecules and was several times lower in intensity than the 1940 nm peak, which formed the most asymmetric and broadest peak, corresponding to molecular water (Integrated Spectronics 1999). The peaks typical for functional groups of Al-OH (2200 nm), Fe-OH (2250 nm), Mg-OH (at 2310 nm) and/or carbonate (CO_3^{2-}) (at 2340 nm) were not visible in the majority of the samples. This can be attributed primarily to the low abundance in samples, and then to the degree of crystallinity of minerals. Poorly crystalline minerals often display weak absorption features, whereas highly crystalline minerals usually show deeper and sharper absorption features.

As an example, representative SWIR-reflectance spectra, obtained for 24 samples from the 3.13 m-long gravity core-627, are shown in Fig. 3. As can be seen, the three consecutive sections at different depths (C: 20 - 120 cm, B: 120 - 218 cm; A: 219 - 313 cm) are heterogeneous: the top 40 cm contain fragments of carbonates of light brown color, which are registered in the first sample shown, i.e., GC-627/C-30, by characteristic diagnostic feature for CO_3^{2-}-stretching at 2340 nm, only feature that persists in mixtures (Fig. 3, 1. GC-627/C-30). Since weaker carbonate absorption features at 1878, 1998 and 2155 nm, do not persist in mixtures, they could not be detected in the most of the studied samples (Horsfall 1999). Carbonate functional group at 2340 nm can be also observed in samples GC-627: C-90, B-146, B-163, B-170, B-175, B-184, B-197, where calcite was also identified by X-ray diffraction analysis (XRD) (Murton et al. 2019; Milinovic et al. 2020). In the majority of hydrothermal samples, the typical band of the reflectance carbonate group was not observed, possibly because of the content of carbonates (mainly calcite), which was not enough to be visible in analyzed sample spectra profiles. In order to test this and to determine the detection limit for calcite, identified by its typical band at 2340 nm, in clay samples, synthetic clay mixtures (containing pure: halite, quartz, montmorillonite, illite and kaolinite) with increasing proportions of calcite (11 - 46 wt.%) were prepared and run by SWIR-analysis. The results of this spectral analysis showed that only clay mixtures containing more than 20 wt.% of calcite, showed a visible, characteristic band at 2340 nm in SWIR-reflectance spectra. Similar results were obtained by Thompson et al. (1999). Thus, in previously mentioned GC-627 samples, more intense characteristic carbonate peak could be observed, because its portion, i.e., most probably in excess of 20 wt.% (Fig. 3, 1. GC-627/C-30, 5. GC-627/C-90, 9. GC-627/B-146, 10. GC-627/B-163, 11. GC-627/B-170, 12. GC-627/B-175, 13. GC-627/B-184, 14. GC-627/B-197).

In some cases, dark (hydrothermal-rich) samples showed very weakly defined spectra, with low signal-to-noise ratios in the range 2300-2500 nm, which are difficult to interpret (Fig. 3, 8. GC-627/C-118, 15. GC-627/B-212, 16. GC-627/B-216, 17. GC-627/A-222, 18. GC-627/A-241, 19. GC-627/A-256, 20. GC-627/A-271, 21. GC-627/A-280, 22. GC-627/A-285, 23. GC-627/A-290, 24. GC-627/A-307). This low signal-to-noise and spectral resolution can be explained by the presence of 'dark' sulfide minerals (e.g., pyrite, chalcopyrite), which do not reflect the radiance in the near infrared-wavelength range (Rona et al. 1996), and hence for dark samples, the spectral region of 2300-2500 nm was characterized with poor reflectance response. To support this hypothesis, the presence of both minerals, pyrite and chalcopyrite was confirmed in listed GC-627 samples: C-118, B-212, B-216, A-241, A-256, A-290, A-307, by XRD-analysis (Murton et al. 2019; Milinovic et al. 2020).

The reflectance spectroscopy of REE-bearing phases is well established in the physico-chemical fields, but naturally occurring REE minerals with variable REE distributions and other elemental substitutions, are relatively poor understood (Turner et al. 2014). In general, the strength of absorption features of REE will be primarily a function of the concentration of the ion and its specific absorptivity within a given crystal structure. The position of the specific REE-related absorption feature will be primarily a function of the cationic coordination and asymmetry in the host crystal structure. Thus, the variations in spectra of REE-bearing minerals are predominantly dependent on the relative strengths of REE-specific absorption features, crystallographic orientation, and variations in other trace elements.

In the study of single-crystal fragments of REE-bearing minerals, it was shown that several sharp absorption features in the SWIR-region can be observed. As an example, the pure oxides Y_2O_3 and Yb_2O_3 show minor absorptions near 1420 nm and 1950 nm (Turner et al. 2016). In spectra shown in Fig. 2, these broad peaks are present in all selected samples and as previously stated, they correspond to hydroxyl group (of water) and water molecule, respectively. Some REE-phosphate minerals, such as monazite and britholite show band also nearly at 1950 nm, related to water (Turner et al. 2016). In the region between 2150 and 2530 nm, some REE-minerals display absorptions related to REE-OH bonding and possible $-CO_3^{2-}$ group, expressed as minima and shoulders, thus making interpretations difficult (Turner et al. 2016). This region is associated with several trivalent lanthanide elements (e.g., La^{3+}, Pr^{3+}, Eu^{3+}), but also with major-element hydroxyl groups, such as Al-OH (2200 nm), Fe-OH (2250 nm), Mg-OH (2310 nm), and carbonate group ($-CO_3^{2-}$) i.e., calcite (2340 nm). Similar to Mg-OH and carbonate group, the pure fluoroapatite is dominated by bands at 2318 and 2499 nm (Gaffey 1986). If absorptions in the infrared region were solely attributed to REE-minerals, the available database with REE-spectral features would be easier to interpret.

Since the selected sediment samples are not monomineralic, their overall spectral features will depend on the composition of all minerals, principally on calcite, goethite, nontronite, pyrite, quartz, etc., that were found in the highest relative content is studied sediment samples (Milinovic et al. 2020). The infrared reflectance is caused by several effects, but the crucial is the abundance of each mineral, the degree of crystallinity and the corresponding reflectance coefficients. The interpretation of spectra of mixed mineral assemblages can have inherent complications because of interfering effects (Kerr et al. 2011). As mentioned earlier, the REE may have distinctive responses in the short-wave infrared regions that could be visible if the concentration of REE-bearing minerals is more than several wt.%, but since in the studied sediment samples the rare earths were found in very low concentrations (up to 35 ppm) compared to other mineral-elements, the REE-characteristic reflectance features could not be interpreted. They were overlapped by typical bands of water molecules and/or major element groups, which contribution was higher due to higher abundance. Nevertheless, the spectral signature of the natural mixtures are empirically useful even if the individual characteristic mineral-element or characteristic group features can't be identified.

3.3 Qualitative statistics: Application of unsupervised principal component analysis

In order to test which mineral components are the key parameters for the cluster analysis of sediment samples, two-factor principal component analysis (PCA) was applied to the referent dataset obtained for the major mineral elements and REE. Over 90% of the variability (PC-1 + PC-2) among the scores of samples (Fig. 4) lies within a plane defined by two linear functions. The first component (PC-1 axes) explained 67% of variance of the data, whereas the second component (PC-2 axes) 24% of variance.

From the correlation loadings plot, it can be observed that PC-1 is dominated by Cu, which is negatively correlated to K, Mg and Si, associated with a few samples near Shimmering mound. On the other hand, Southern mound sediments are characterized with higher levels of Mn, whereas at Shimmering mound, Si-containing samples predominate. Moreover, it can be noticed that, except Eu, all REE are clustered in the first quartile of the diagram, showing positive contributions to both axes (PC-1 and PC-2) that are linearly correlated with sediments from the MIR zone, Shimmering, Rona and Southern mounds.

3.4 Quantitative statistics: From screening to quality control analysis of mineral components and REE in TAG-sediment samples

A quantitative and full cross-validation partial least square regression (CVPLSR) model that could enable reliable estimations of total content of mineral components was applied to reflectance SWIR-spectra of all samples with known geochemical composition. The optimal results were selected according to the statistical parameters obtained, considering the most adequate those with higher coefficient of determination (R^2) and lower root mean square error (RMSE) values from regression analysis. Hence, in case of Cu, Mn, Pb, S, and Zn, the model could not provide satisfactory statistical results, due to very high concentrations of these elements found in sediment samples. Namely, mean Pb concentration was approximately 80 ppm, whereas for the rest of the elements (i.e., Cu, Mn, S, and Zn), the mean concentrations were higher than 2,400 ppm. Hence, the calibration models for these elements could lead to erroneously overestimation in comparison with other elements.

Considering Al, Ca, Fe, K, Mg, and Si determination, the CVPLSR model gave satisfactory statistics and the values of latent variables (LV), coefficient of determination (R^2) and root mean square error for calibration (RMSEC) and cross-validation (RMSECV) data sets are presented in Table 2. As can be observed, minimal number of latent variables was 3 for the Al regression model, and 5 variables were sufficient to explain the K regression model. For the rest of mineral components, 7 latent variables were necessary to maximize the relationship between independent (referent value) and dependent variables (predicted value). The coefficients of determination were in range from 0.52 to 0.94 (Ca) and standard error (RMSE) lower than 3.29 and 5.94 (Fe) for calibration and cross-validation set of data, respectively. The regression models in here were characterized by residual predictive deviation (RPD) statistic, used as a method for evaluation of the quality of applied regression analysis. The RPD values for calibration were in range from 1.44 for the total content of Al, until 4.25 for Ca content. The RPD values of calibration data set for Ca, Fe, and Si had values higher than 2.50, which means that applied model provided satisfactory results for screening purposes of these elements by SWIR. Our results showed better statistics, with higher RPD values in comparison with some other available results. As an example, the values of RPD for Ca, Fe, and Si in lake and ditch sediment samples from the Netherlands, were equal to 2.1, 2.2 and 1.8, respectively, and thus they couldn't allow significantly good screening of tested sediments (Kleinbecker et al. 2013). For the rest of the elements studied, such as Al, K and Mg, our results are similar to previously published ones, ranging from 1.44 (Al) to 1.98 (Mg), i.e., calibration models allowed good approximation of quantitative predictions (Kleinbecker et al. 2013).

After excluding an outlier sample (GC-644/A-225), (n = 64), the RPD value of applied model for Ca was higher than 5, i.e., RPD = 5.51. This unequivocally allows the model to be used for the quality control of Ca concentration in sediments by SWIR-analysis. This can be particularly important for samples containing Ca-bearing minerals, such as calcite, dolomite and magnesite. As an example, the optimized multivariate CVPLSR-model for determination of Ca, calibration and cross-validation statistics, are presented in Fig. 5. Very good statistics are obtained for the 64 samples tested, with high coefficient of determination ($R^2 = 0.97$) between predicted and referent values of Ca. Moreover, root mean square errors and standard errors of calibration were less than 2, and bias was negligible. Hence, obtained result can be assumed as satisfactory in comparison with scarce data available in the literature. Similar plots that demonstrate good fits of the CVPLSR model for Si quantification are presented in Fig. 6. The results showed higher dispersion with lower coefficient of determination ($R^2 = 0.88$) in comparison with Ca, and this can be explained by less concentration of Si (more than twice the Ca concentration) and by lower diagnostic absorption of Si-bearing minerals, in the broad zone of approximately 1400 nm (Horsfall 1999).

Taking into account REE, without Eu (for which the PCA also showed exception, with respect to cluster of the other REE, grouped together), all regression models of their concentrations were found to be acceptable. Relatively good statistics in most of the samples (n = 64), were characterized with high coefficients of determination ($R^2 > 0.73$) and the RPD values for calibration dataset were in the range from 1.90 (Sm) to 2.42 (Ce) (Table 3). After excluding two outliers (GC-682/B-116 and GC-692/A-43), the values of R^2, RMSE and RPD did not change significantly, with an exception, for Ce and Er, which determinations gave better statistics with higher values of RPD (2.55 and 2.59, respectively), thus providing the use of SWIR-spectral data for screening purposes of two rare earth elements. The optimized multivariate CVPLSR-model for the determination of Ce and Er, calibration, and validation statistics, are presented in Fig. 7 and Fig. 8, respectively. Very good statistics were obtained for the 62 samples tested and in general, the results can be assumed as satisfactory taking into account that there is no data available in the literature. Summarizing, obtained results demonstrate a good correlation between mineral components and SWIR-reflectance data by cross-validation PLSR-multivariate analysis. The relatively high RPD-values enable us to evaluate the mineral components and REE in studied TAG sediments by SWIR analysis.

4 Conclusions

Rapid, non-destructive and economically acceptable SWIR-reflectance analysis provided representative statistics for the evaluation of geochemical variables in sediment samples from the TAG hydrothermal field. Based on the established modeling equations, one can substitute time-consuming destructive sample preparation (digestion/extraction procedure) and conventional analytical methods (ICP/OES and ICP/MS) by reliable SWIR-spectral analysis to get both qualitative and quantitative results of mineral components and geochemistry in deep-ocean sediment samples.

The work described in here, successfully demonstrated the potential usefulness of SWIR-spectral data combined with an appropriated multivariate regression model for the quantification of mineral components and REE in sediment samples, when time and costs are limiting factors. As strategic elements with recently high demands, the REE can be explored with SWIR-reflectance spectra that can provide information of their content in near-real time, with significant implications for their beneficiation. Future studies will include more gravity core samples hosted in deep-ocean sediments which may improve proposed CVPLSR models.

Acknowledgments

The work was done as part of the project "BLUE MINING - Breakthrough solutions for the sustainable exploration and extraction of deep-sea mineral resources", that has received funding from the European Union's Seventh Framework Programme for research, technological development and demonstration under Grant agreement Nº 604500. The authors would like to acknowledge the financial support FCT through project UIDB/50019/2020 – IDL.

The authors would like to thank to Dr Sven Petersen (GEOMAR, Helmholtz Center for Ocean Research, Kiel, Germany), Dr Sofia Martins and to the 'M127' cruise team, for technical support during the oceanographic mission, gravity cores recovering, their preservation a priori de analysis, and for the AUV-derived, map of the TAG hydrothermal field.

The authors are specially thankful to Editor-in-Chief of the Journal, Subject Editor, and to Referees for their constructive and valuable comments, which improved the manuscript until its final version.

Compliance with ethical standards

The authros declare no conflicts of interest. The research did not involve any studies with human participants and/or animals. Informed consent was obtained from all individual participants included in the study.

References

Actlabs (2019) Euro schedule of services, http://www.actlabs.com/. Accessed 07 April 2019

Barriga FJAS (2017) Can recycling and the circular economy render seafloor mining unnecessary? Economical, Technological and Environmental Aspects: Cooperative Solutions for Future Deep-sea Mining Underwater Mining Conference, Federation of German Industries (BDI), Berlin, Germany

Blengini GA, Nuss P, Dewulf J, Nita V, Talens Peiro LT, Vidal-Legaz B, Latunussa C, Mancini L, Blagoeva D, Pennington D, Pellegrini M, Van Maercke A, Solar S, Grohol M, Ciupagea C (2017) EU methodology for critical raw materials assessment: Policy needs and proposed solutions for incremental improvements. Resour Policy 53:12-19

Campbell AC, Palmer MR, Klinkhammer GP, Bowers TS, Edmond JM, Lawrence JR, Casey JF, Thompson G, Humphris S, Rona P, Karson JA (1988) Chemistry of hot springs on the Mid-Atlantic Ridge. Nature 335:514-519

Carvalho CMN, Barriga FJAS (2000) Preliminary report on the mineralogical detailed study at the alterations zones surrounding the Feitais VMS ore body (Aljustrel, Portugal, IPB), in: Proceedings International Conference and Field Meeting on Volcanic environments and Massive Sulfide Deposits, CODES Special Publication, 3:19-21

Christie T, Brathwaite B, Tulloch A (1998) Mineral Commodities Report 17 - Rare Earths and Related Elements. New Zealand Institute of Geological and Nuclear Sciences Limited pp. 1-13

Clark RN, King TVV, Klejwa M, Swayze GA (1990) High spectral resolution reflectance spectroscopy of minerals. J Geophys Res 95:12653-12680

Coulomb R, Dietz S, Godunova M, Nielsen TB (2015) Critical minerals today and in 2030: An analysis for OECD countries, OECD environment working papers, OECD Publishing, Paris, no. 91:1-50

German CR, Higgs NC, Thomson J, Mills R, Elderfield H, Blusztajn J, Fleer AP, Bacon MP (1993) A geochemical study of metalliferous sediment from the TAG hydrothermal mound, 26°08'N, Mid-Atlantic Ridge. J Geophys Res 98:9683-9692

German CR, Klinkhammer GP, Edmond JM, Mura A, Elderfield H (1990) Hydrothermal scavenging of rare-earth elements in the ocean. Nature 345:516-518

Hein JR, Mizell K, Koschinsky A, Conrad TA (2013) Deep-ocean mineral deposits as a source of critical metals for high- and green-technology applications: Comparison with land-based resources. Ore Geol Rev 51:1-14

Horsfall C (1999) Short wave infrared spectroscopy for geological mapping and mineral exploration using the PIMA field portable spectrometer. PIMA SP and PimaView 3.1 Integrated Spectronics (6th ed) Pty Ltd. North Ryde NSW, 2113, Australia, pp. 1-77

Elderfield H, Hawkesworth CJ, Greaves MJ, Calvert SE (1981) Rare earth element geochemistry of oceanic ferromanganese nodules and associated sediments. Geochim Cosmochim Acta 45:513-528

Emsbo P, McLaughlin PI, Breit GN, du Bray EA, Koenig AE (2015) Rare earth elements in sedimentary phosphate deposits: Solution to the global REE crisis? Gondwana Res 27:776-785

European Commission (2017) Study on the review of the list of Critical Raw Materials, Executive summary report. DG for Internal Market, Industry, Entrepreneurship and SMEs, Brussels, Sep. pp. 1-9

Gaffey SJ (1986) Spectral reflectance of carbonate minerals in the visible and near infrared (0.35-2.55 microns); calcite, aragonite, and dolomite. Am Mineral 71:151-162

Giese EC (2018) Rare earth elements: Therapeutic and diagnostic applications in modern medicine. Clin Med Rep 2:1-2

Integrated Spectronics (1999) Short Wave Infrared Spectroscopy for Geological Mapping and Mineral Exploration Using the Pima Field Portable Spectrometer 6th edition of Pima SP and Pima View User Manual, Baulkan Hills, NSW, Australia, p 72

Kerr A, Rafuse H, Sparkes G, Hinchey J, Sandeman H (2011) Visible/Infrared spectroscopy (VIRS) as a research tool in economic geology: Background and pilot studies from Newfoundland and Labrador. Current Research, Geological Survey Report 11:145-166

Kleinebecker T, Poelen MDM, Smolders AJP, Lamers LPM, Hölzel N (2013) Fast and inexpensive detection of total and extractable element concentrations in aquatic sediments using near-infrared reflectance spectroscopy (NIRS). PLoS ONE 8:e70517

Koeppenkastrop D, De Carlo EH (1992) Sorption of rare-earth elements from seawater onto synthetic mineral particles: An experimental approach. Chem Geol 95:251-263

Lorenz S, Beyer J, Fuchs M, Seidel P, Turner D, Heitmann J, Gloaguen R (2019) The potential of reflectance and laser induced luminescence spectroscopy for near-field rare earth element detection in mineral exploration. Remote Sens 11:21

Lusty PAJ, Murton BJ (2018) Deep-ocean Mineral Deposits: Metal resources and windows into Earth processes. Elements 14:301-306

Milinovic J, Dias ÁA, Janeiro AI, Pereira MFC, Martins S, Petersen S, Barriga FJAS (2020) XRD identification of ore minerals during cruises: Refinement of extraction procedure with sodium acetate buffer. Minerals 10:160

Mills R, Elderfield H, Thomson J (1993) A dual origin for the hydrothermal component in a metalliferous sediment core from the Mid-Atlantic Ridge. J Geophys Res 98:9671-9681

Murton BJ, Berit L, Dutrieux AM, Martins S, de la Iglesia AG, Stobbs IJ, Barriga FJAS, Bialas J, Dannowski A, Vardy ME, North LJ, Yeo IALM, Lusty PAL, Petersen S (2019) Geological fate of seafloor massive sulphides at the TAG hydrothermal field (Mid-Atlantic Ridge). Ore Geol Rev 14:903-925

Petersen S (2017) Metal fluxes and resource potential at the slow-spreading TAG mid-ocean ridge segment (26°N, MAR) – Blue Mining @ Sea, Cruise No. M127, Bridgetown (Barbados) - Ponta Delgada (Portugal), May 25 - June 28, 2016. RV METEOR, Cruise report M127 (extended version), GEOMAR pp. 1-59

Petersen S (2016) News from the seabed - Geological characteristics and resource potential of deep-sea mineral resources. Mar Policy 70:175-187

Petersen S, Yeo I, Jamieson J, Szitkar F, Graber S, Augustin N, Rothenbeck M, RV Meteor Scientific Part (2017) AUV-based exploration of the TAG segment at 26°N, Mid-Atlantic ridge: Implications for resource assessment and metal fluxes. Goldschmidt Abstracts, Paris, France, 3135

Rona PA, Klinkhammer G, Nelsen JA, Trefry JH, Elderfield H (1986) Black smokers, massive sulphides and vent biota at the Mid-Atlantic Ridge. Nature 321:33-37

van Ruitenbeek FJA, Cudahy TJ, Van der Meer FD, Hale M (2012) Characterization of the hydrothermal systems associated with Archean VMS-mineralization at Panorama, Western Australia, using hyperspectral, geochemical and geothermometric data. Ore Geol Rev 45:33-46

Sun Y, Seccombe K, Yang K (2001) Application of short-wave infrared spectroscopy to define alteration zones associated with the Elura zinc-lead-silver deposit, NSW, Australia. J Geochem Explor 73:11-26

Thompson AJB, Hauff PL, Robitaille AJ (1999) Alteration mapping in exploration: application of short-wave infrared (SWIR) spectroscopy. SEG Newsletter 39:16-27

Thompson G, Mottl MJ, Rona PA (1985) Morphology, mineralogy and chemistry of hydrothermal deposits from the TAG area, 26°N Mid-Atlantic ridge. Chem Geol 49:243-257

Turner DJ, Rivard B, Groat LA (2014) Visible and short-wave infrared reflectance spectroscopy of REE fluorocarbonates. Am Mineral 99:1335-1346

Turner DJ, Rivard B, Groat LA (2016) Visible and short-wave infrared reflectance spectroscopy of REE phosphate minerals. Am Mineral 101:2264-2278

Van Dover CL (2019) Inactive sulfide ecosystems in the deep sea: A review. Front Mar Sci. https://doi.org/10.3389/fmars.2019.00461

Williams PC, Sobering DC (1993) Comparison of commercial near infrared transmittance and reflectance instruments for analysis of whole grains and seeds. J Near Infrared Spec 1:25-32

Figs. (1 - 8)

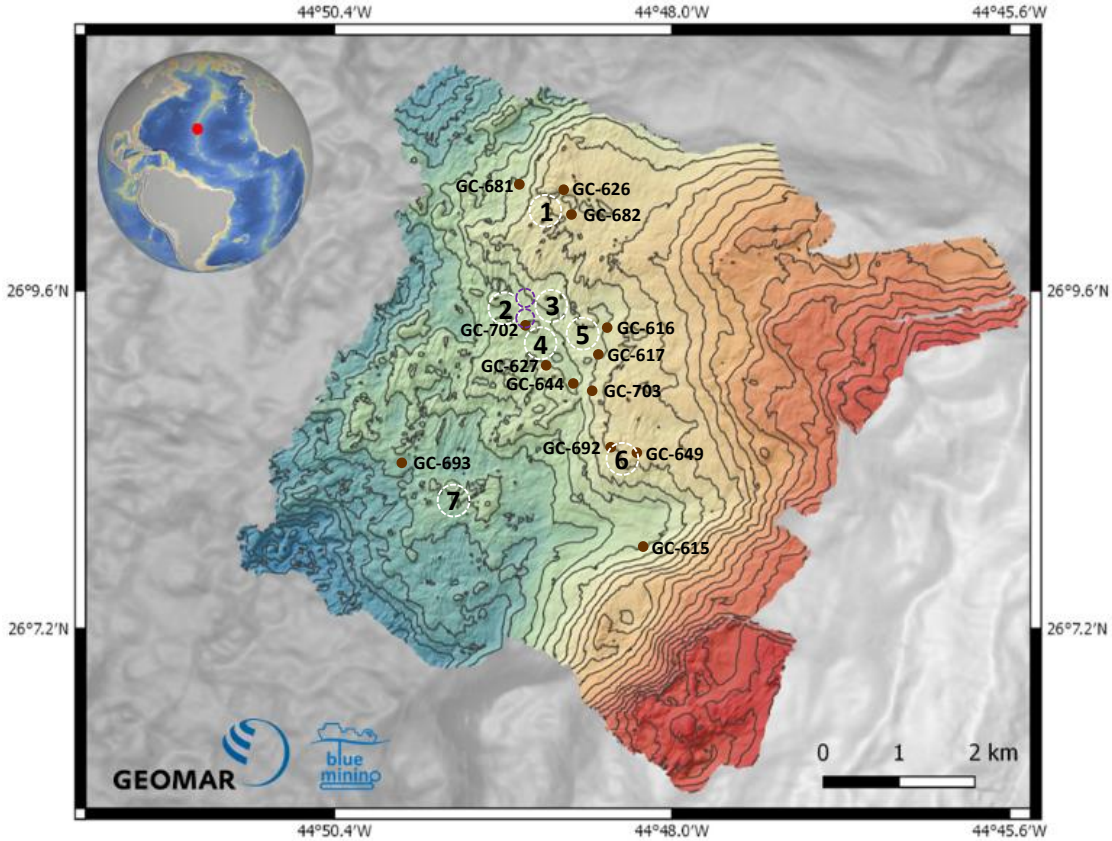

Fig. 1 Location of gravity cores recovered during 'M127' at the TAG hydrothermal field. AUV-derived map produced by GEOMAR (Petersen 2017). 1. Shimmering mound 2. Shinkai mound 3. Double mound 4. Southern mound 5. Rona mound 6. MIR zone 7. TAG active mound

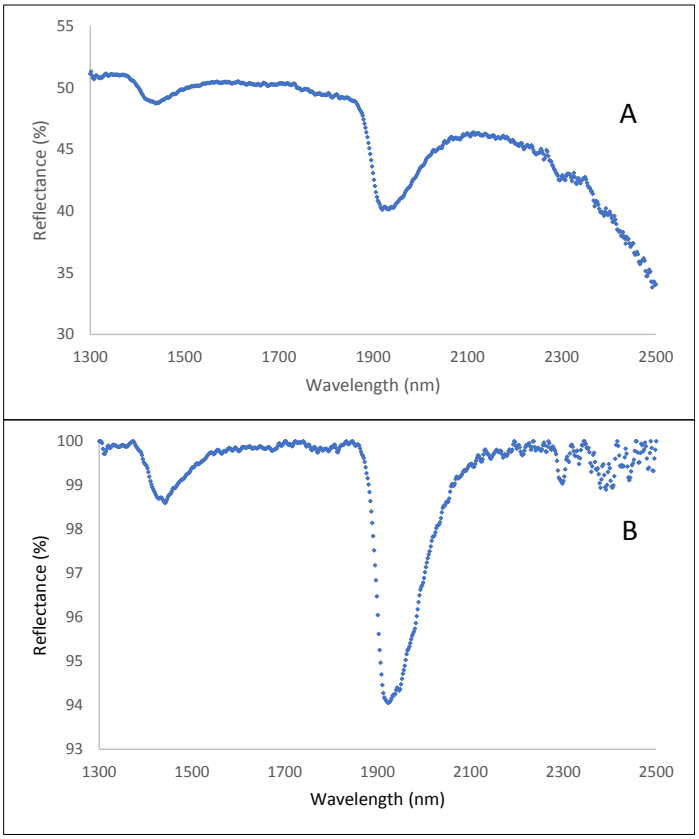

Fig. 2 Original, raw reflectance (A) and hull-quotient (B) SWIR-spectra of sample GC-627/B-175. By dividing the reflectance spectrum by the baseline at each wavelength, the effect of background is removed and the hull-quotient spectrum is derived. Note that the minor features (at 2300 nm) in original reflectance spectrum became more emphasized in the hull-quotient spectrum

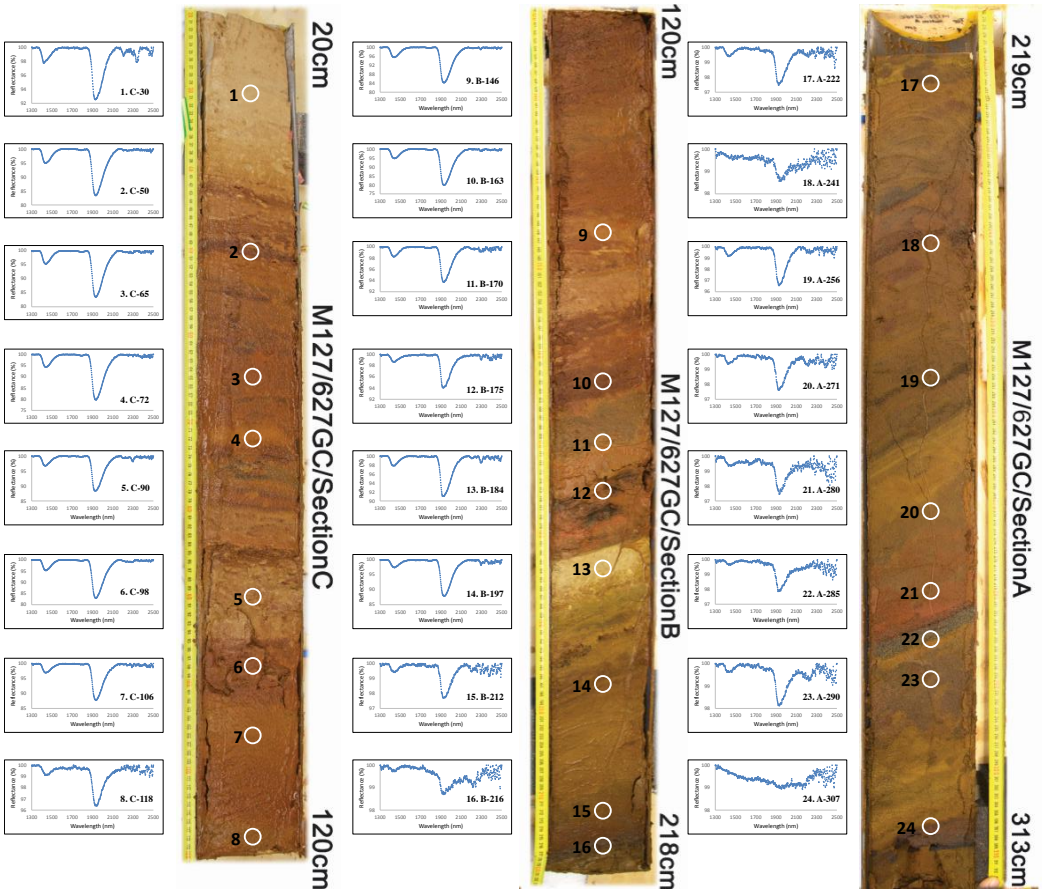

Fig. 3 Hull-quotient SWIR-reflectance spectra of selected samples from the GC-627 (Sections: C, B, A), gravity cored proximal to Southern mound. Each SWIR-spectrum corresponds to sampling point (white circle) indicated in cored sediment image. Shape and reflection features of spectra correspond to the mineral composition in selected samples (core images were made offshore)

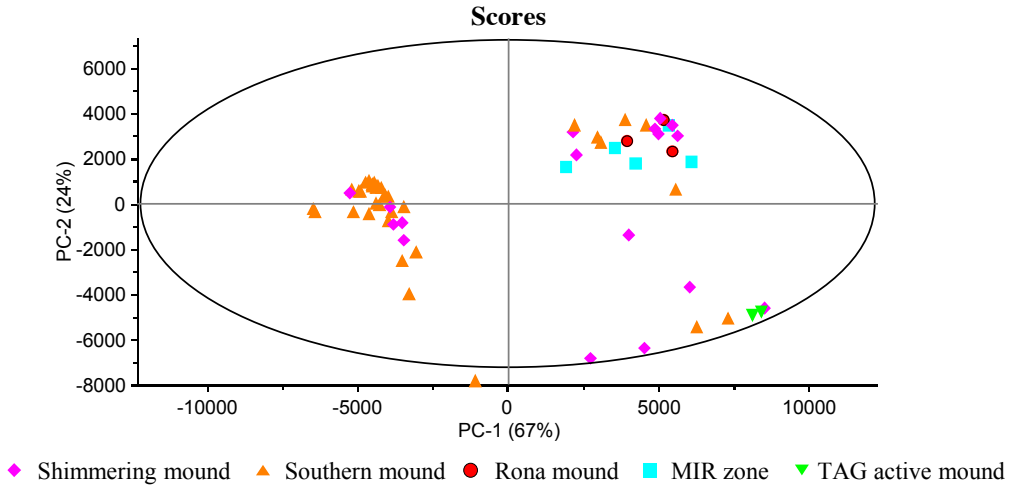

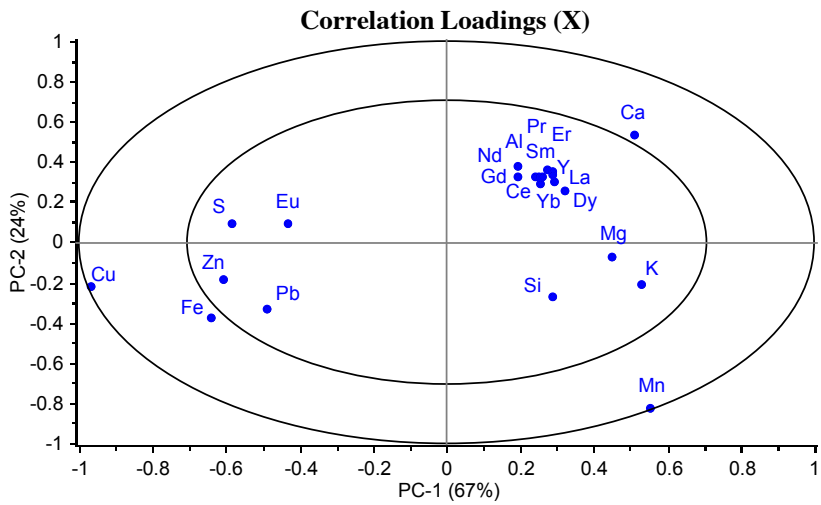

Fig. 4 Original PCA plots of analyzed GC-sediment samples (n = 64) based on their geochemical data (variables): Scores plot of the first two principal components show the clustering of samples, while Correlation Loadings plot reflect the influence of variables and the correlations between them

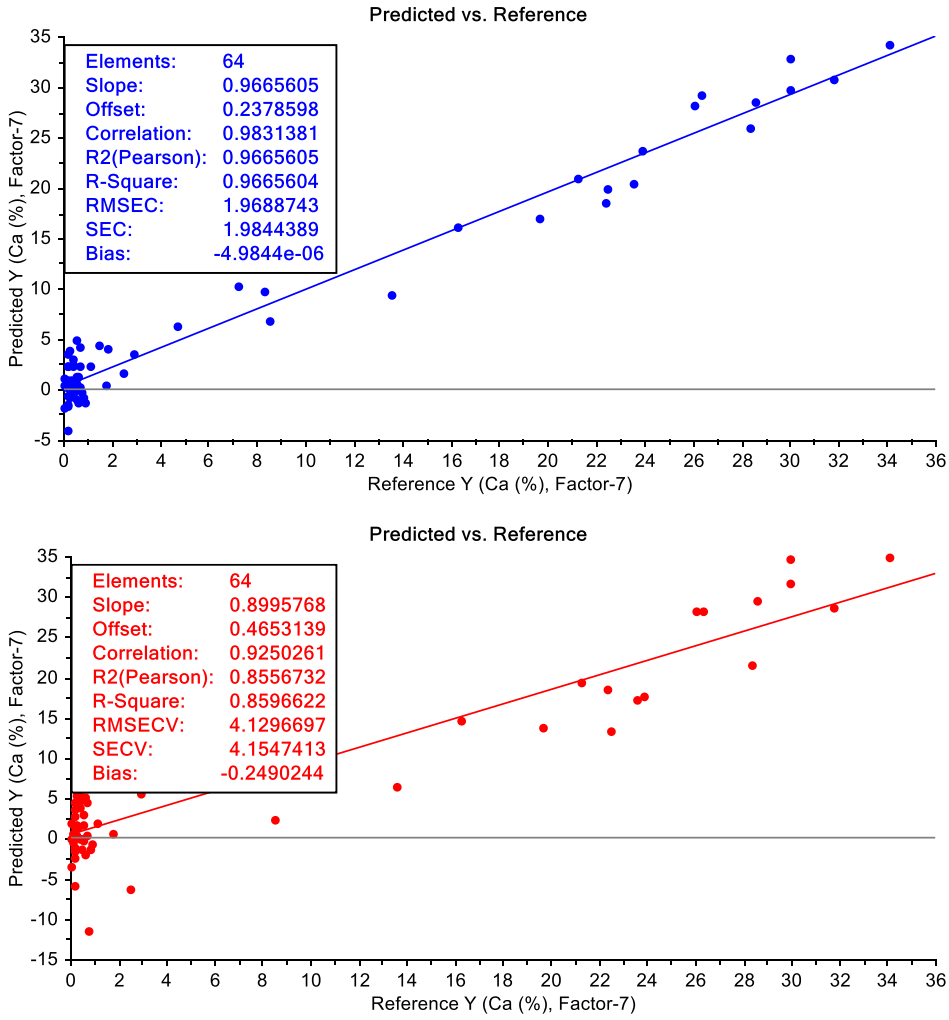

Fig. 5 Original plots obtained for CVPLSR model (calibration - A and validation - B) for predicted Ca content (%) in TAG sediment samples (n = 64) vs. referent values obtained by ICP-analysis. Seven latent variables (factor = 7) were used to maximize covariance between predicted and referent dataset. The inserted squares contain statistical parameters that explain quantitatively the goodness of model. Slope and offset (intercept) define the linear relationship between two variables of the regression line. High values of coefficient of determination ($R^2 = 0.86$), together with low values of root mean square error of calibration (RMSEC = 2) and cross-validation (RMSECV = 4), described strong relationship between predicted and referent values for Ca. Minimal value of bias (negligible value for calibration and near-to-zero value for validation dataset) additionally confirmed the goodness of fitted model

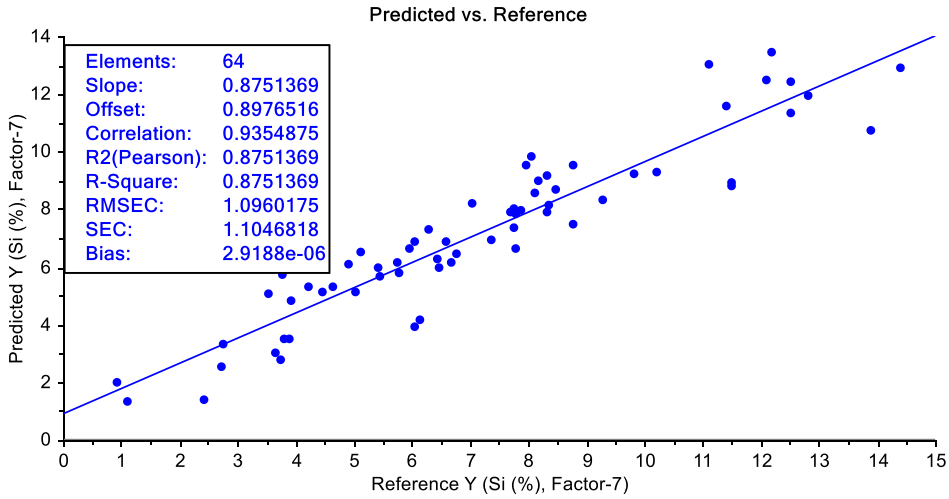

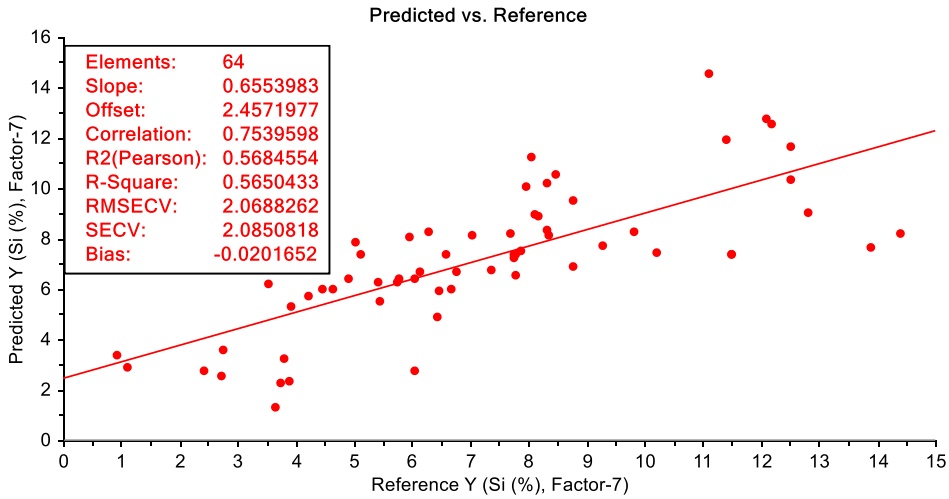

Fig. 6 Original plots obtained for CVPLSR model (calibration - A and validation - B) for prediction of Si content in TAG sediment samples (n = 64). Inserted squares contain the statistical parameters of the model (the explanation of the relevant parameters used for statistical analysis of data, is given in detail in Fig. 5)